JOURNAL OF SPACECRAFT AND ROCKETS
Vol. 36, No. 3, May–June 1999

Aerothermal Heating Predictions for Mars Microprobe

R. A. Mitcheltree,* M. DiFulvio,* T. J. Horvath,* and R. D. Braun†
NASA Langley Research Center, Hampton, Virginia 23681

A combination of computational predictions and experimental measurements of the aerothermal heating expected on the two Mars Microprobes during their entry to Mars is presented. The maximum, nonablating heating rate at the vehicle's stagnation point (at zero angle of attack) is predicted for an undershoot trajectory to be 194 W/cm² with associated stagnation-point pressure of 0.064 atm. Maximum stagnation-point pressure occurs later during the undershoot trajectory and is 0.094 atm. From computations at seven overshoot-trajectory points, the maximum heat load expected at the stagnation point is near 8800 J/cm². Heat rates and heat loads on the vehicle's afterbody are much lower than on the forebody. At 0-deg angle of attack, heating over much of the hemispherical afterbody is predicted to be less than 2% of the stagnation-point value. Good qualitative agreement is demonstrated for forebody and afterbody heating between computational fluid dynamics calculations at Mars entry conditions and experimental thermographic phosphor measurements from the NASA Langley Research Center 20-Inch Mach 6 Air Tunnel. A novel approach that incorporates six-degree-of-freedom trajectory simulations to perform a statistical estimate of the effect of angle of attack and other off-nominal conditions on heating is included.

Nomenclature

B = ballistic coefficient, kg/m²
C_h = heat transfer coefficient
M = Mach number
P = pressure, atm
q = heat rate, W/cm²
Re = Reynolds number
R_n = nose radius, m
s = surface distance from geometric stagnation point, m
t = independent variable time, s
V = velocity, m/s
x, z = independent spatial dimensions, m
α = angle of attack, deg
β = sideslip angle, deg
γ = inertial flight path angle, deg
ρ = density, kg/m³
σ = standard deviation

Introduction

WHEN the Mars Surveyor 1998 Lander is launched in January 1999, there are plans to transport not only its own lander to Mars, but two small soil penetrators. These two Mars Microprobes[1] are the second of the Deep Space missions from NASA's New Millennium Program Office. Upon arrival at Mars, the penetrators will be released from the cruise stage and begin a free fall to the surface. This paper focuses on predicting the convective heating that the aeroshells will encounter during the hypersonic portion of that Mars entry. Knowledge of the expected heating is necessary to design forebody and afterbody thermal protection systems (TPSs).

Both computational fluid dynamics (CFD) predictions and experimental measurements are presented. The quantitative analysis focuses on computational predictions for heating at 0-deg angle of attack. Solutions are generated at the estimated maximum heating point for an undershoot trajectory. This solution estimates the maximum instantaneous heating the TPS should encounter and aids in selection of the appropriate TPS material. Seven points from an overshoot trajectory are then examined to establish the temporal variation in heating and the integrated heat load that is used to specify the TPS thickness. Afterbody heating is examined through a combination of computational predictions and experimental measurements. Finally, statistical six-degree-of-freedom (DOF) trajectory simulations are combined with experimental and computational heating predictions to establish the effect of angle of attack on heating and overall heat load.

Microprobe Geometry

The forebody geometry for Mars Microprobe is geometrically similar to that used for the small probes in the 1978 Pioneer Venus mission.[2] It is a 45-deg half-angle sphere–cone with nose radius equal to half the base radius. The shoulder radius is $\frac{1}{10}$th the nose radius. For Microprobe, the base radius is 0.175 m, the nose radius is 0.0875 m, and the shoulder radius is 0.00875 m.

The aeroshell geometry is shown in Fig. 1. The afterbody is hemispherical with the radius at the center-of-gravity location. This hemispherical afterbody shape is much larger than that used on the Pioneer Venus probes. Selection of the aeroshell is discussed in Ref. 3.

Entry Trajectories

Predicting heating on the Microprobe aeroshells during their entry at Mars requires knowledge of the expected entry trajectory. Six-DOF entry trajectory simulations were performed using POST[4] with an aerodynamic database comprising free-molecular, direct simulation Monte Carlo calculations, CFD calculations, wind-tunnel data, and ballistic-range data. The creation of the aerodynamic database is discussed in Ref. 3. Velocity at atmospheric interface is assumed to be 6.90 km/s. The nominal inertial entry angle γ is -13.25 deg at a radius of 3522.2 km.

With respect to heating, the major uncertainties in the trajectory simulation are the entry angle at atmospheric interface and the vehicle mass. For heatshield design, the vehicle mass is assumed to be 3.84 kg, which represents a ballistic coefficient of 38 kg/m². (Nominal mass is 3.405 kg for a ballistic coefficient of 33.7 kg/m².) The uncertainty in the entry angle is ± 0.4 deg. Thus, in addition to a nominal trajectory, undershoot and overshoot trajectories are predicted by POST with entry angles of -13.65 and -12.85 deg, respectively.

Stagnation-point heating to a sphere can be estimated from a Sutton–Graves[5] predictor. The Sutton–Graves correlation for the Mars atmosphere (97% CO_2 and 3% N_2 mass fractions) at this direct entry condition is

$$q_s = 1.89 \times 10^{-8} R_n^{-0.5} \rho_\infty^{0.5} V_\infty^3 \qquad (1)$$

where ρ_∞ and V_∞ are the freestream density and velocity in kilograms per cubic meters and meters per second, respectively, and

Received Jan. 10, 1998; presented as Paper 98-0170 at the AIAA 36th Aerospace Sciences Meeting, Reno, NV, Jan. 12–15, 1998; revision received Aug. 15, 1998; accepted for publication Feb. 22, 1999.

*Aerospace Engineer, Aerothermodynamics Branch, Aero and Gas Dynamics Division. Senior Member AIAA.

†Aerospace Engineer, Vehicle Analysis Branch, Space Systems and Concepts Division. Member AIAA.

Table 1 Maximum heating point (undershoot trajectory)

t, s	Altitude, km	M	V, m/s	ρ, kg/m^3
78.9	46.2	30.3	5942.8	1.9257e−04

Table 2 Overshoot trajectory points

t, s	Altitude, km	M	V, m/s	ρ, kg/m^3
51.7	76.7	36.2	6908.7	3.882e−06
65.6	63.7	35.0	6809.6	2.032e−05
74.6	56.5	33.7	6614.7	5.099e−05
87.5	47.9	30.4	5956.3	1.549e−04
99.6	41.9	24.6	4864.4	3.263e−04
107.5	39.0	20.4	4053.7	4.665e−04
118.4	35.8	15.2	3054.8	6.695e−04

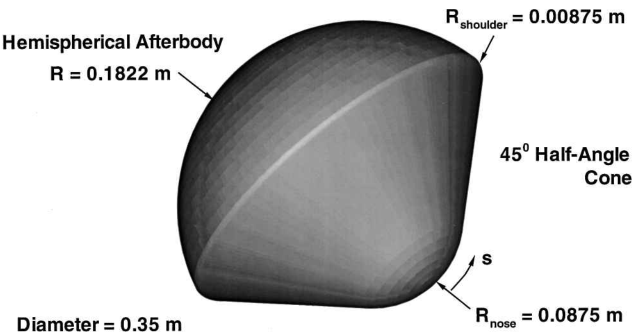

Fig. 1 Geometry of Microprobe aeroshell.

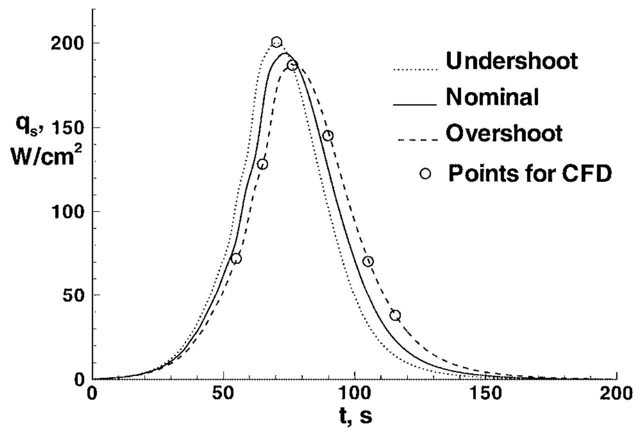

Fig. 2 Sutton–Graves[5] stagnation-point heating estimate for heat-shield design trajectories with $B = 38$ kg/m^2.

q_s is in watts per square centimeter. Heating estimates for the three trajectories using nose radius as the radius in this relation are plotted in Fig. 2. (Time zero is the atmospheric interface initiation of the simulations.) The maximum heat rate expected for Microprobe occurs around $t = 78.9$ s for the undershoot trajectory. The conditions associated with this point are given in Table 1 and will be examined in detail using CFD. Maximum integrated heat load for Microprobe occurs for the overshoot trajectory. Seven points are examined in detail for this trajectory. Those trajectory points are indicated in Fig. 2 and listed in Table 2.

Because Microprobe encounters the Mars atmosphere while tumbling, its attitude at atmospheric interface is unknown. The three reference trajectories discussed earlier assume the vehicle is at 0-deg angle of attack. If the vehicle encounters the atmosphere while traveling at some other attitude, for example, backward, the aeroshells will reorient themselves forward but nonzero angles-of-attack oscillations may persist through some part of the heat pulse. It is necessary to assess the impact of these nonzero angle-of-attack attitudes on heating. To accomplish this, a statistical set of six-DOF trajectory simulations is computed by varying the initial attitude over its expected range of values. Discussion of these trajectories and how a combination of computational and experimental results are used to accomplish this objective are included in the Results section.

Computational Method

The LAURA CFD code was used to predict the heating on Microprobe. LAURA is an upwind-biased, point-implicit relaxation algorithm[6] for obtaining the numerical solution to the Navier–Stokes equations for three-dimensional viscous hypersonic flows in thermochemical nonequilibrium. The Mars atmosphere version of the code[7] contains an eight-species CO_2–N_2 chemical-kinetics model. This is the same computational code used to make aerodynamic and heating predictions for Mars Pathfinder.[8–11] Aerodynamic predictions from the code have agreed well with Viking flight data[11] and have shown to be in excellent agreement with Mars Pathfinder flight data.[12] Nonablating, fully catalytic wall boundary conditions at radiative equilibrium wall temperatures are used in the present study.

Computational grids for the axisymmetric forebody solutions included 30 cells along the forebody and 64 cells normal to the wall, with the first cell off the wall spaced so that the cell Reynolds number is 1. A comparison to a grid with twice as many points in each direction is included in the Results section. The afterbody axisymmetric calculation utilized a 160×64 grid. The three-dimensional forebody calculations used a surface mesh of 59×28 cells with 64 cells normal to the wall.

Mach 6 Air Heating Measurements

In an effort to assess the shoulder region and near afterbody heating rates and heat loads associated with large angles of attack, wind-tunnel tests were conducted in the NASA Langley Research Center 20-Inch Mach 6 Air Tunnel. The objective of the tests was to provide qualitative information on the variation of heating distribution over a large range of angles of attack.

The facility is a blow-down wind tunnel that uses dry air as the test gas. The air can be heated to a maximum temperature of 1088°R by an electrical resistance heater, and the maximum reservoir pressure is 525 psi. A fixed-geometry, two-dimensional, contoured nozzle with parallel side walls expands the flow to Mach 6 at the 20-in. square test section. This tunnel is capable of injecting heat transfer models from a sheltered position to the nozzle centerline in less than 0.6 s. The run time for this facility varies from 2 to 10 min. A description of the facility and calibration results are presented in Ref. 13.

Table 3 presents the conditions for the Microprobe tests measured about a 4-in.-diam fused silica quartz ceramic model. The model was attached to the sting in such a way as to minimize sting interference effects over the angle-of-attack range from 0 to 45 deg.

The relative-intensity two-color thermographic phosphor technique[14] was used to measure surface heat transfer to the model. When illuminated with ultraviolet light, electrons within the phosphor coating are excited and emit visible light during their subsequent relaxation to lower energy levels. The probability that this relaxation occurs is temperature dependent. A true-color-separation camera is used to record the emissions from which quantitative temperature information and, thus, heat transfer can be determined. The camera was positioned to view the windside of the model's forebody and afterbody when at angle of attack.

The validity of using Mach 6 air measurements to provide qualitative information about the heating distribution on a vehicle traveling Mach 30 in Mars's CO_2 atmosphere is uncertain. A comparison with CFD prediction at zero angle of attack is included in the next section.

Results

Computational solutions at 0-deg angle of attack for the undershoot and overshoot trajectories are presented first. An assessment of afterbody heating is next, followed by a discussion of angle-of-attack effects. The experimental measurements are included in the discussions of afterbody heating and angle-of-attack effects.

Table 3 Freestream conditions for Mach 6 air heating measurements

T, K	M	V, m/s	ρ, kg/m^3	Re_∞/ft
62.7	5.97	948.0	6.241e−02	4.3e+06

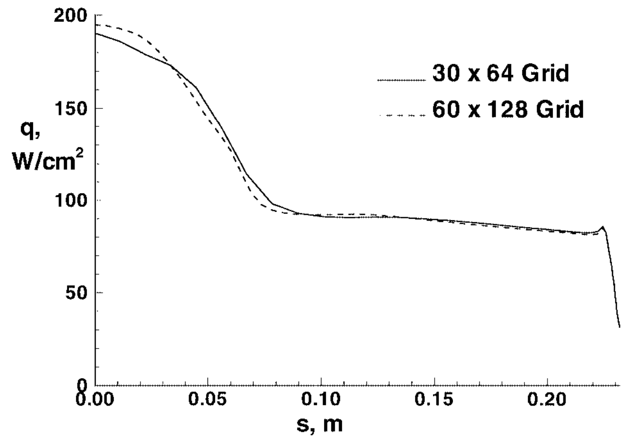

Fig. 3 Forebody heating distribution for maximum heating point on undershoot trajectory.

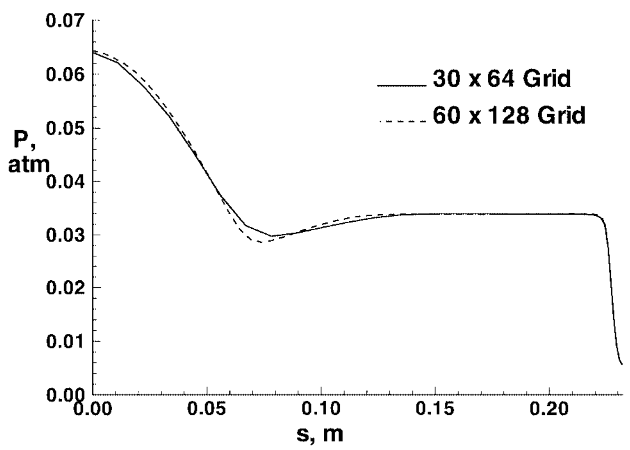

Fig. 4 Forebody pressure distribution for maximum heating point on undershoot trajectory.

Maximum Heating

Figure 3 presents the laminar, nonablating, zero angle of attack, forebody heating predicted at the undershoot trajectory's maximum heating point (Table 1) with a 30×64 grid and a 60×128 grid. Good agreement is observed between the predictions from the two grids. The stagnation-point heating prediction is 194 W/cm^2 on the finer grid, which is 3.6% higher than the approximation from Eq. (1). The prediction for the 30×64 grid agrees with the finer grid prediction except it is 2% lower at the stagnation point.

Heating on the forebody conical flank is about half the stagnation-point value. There is no appreciable rise in heating predicted on the shoulder. Radiative heating is estimated, using the Tauber–Sutton[15] equilibrium method, to be less than 1% of the convective heating presented. It can, therefore, be neglected in sizing the heatshield. Figure 4 presents the forebody pressure distribution associated with the two calculations. The stagnation-point pressure is 0.064 atm. Maximum stagnation-point pressure occurs at $t = 91.5$ s in the undershoot trajectory with a value of 0.094 atm.

An independent check on the stagnation-point maximum heating was performed by using Mars atmosphere chemistry in a viscous shock layer (VSL) code.[16] This method accounts for thermochemical nonequilibrium conditions in the shock layer and includes a 16-species kinetics model of which the 8-species model used in LAURA is a subset. The additional species allow for ionization. The nonablating wall temperature is set to its radiative equilibrium value, and recombination at the surface is assumed to return the mixture to its equilibrium composition at the wall pressure and temperature. This method predicts stagnation-point heating (nonablating) at 178 W/cm^2 with no appreciable ionization. This prediction is 7% lower than the LAURA prediction. The lower VSL prediction results from a lesser degree of wall recombination predicted by the equilibrium assumption at the wall. Temperature at the wall is 2485 K, which results in a CO_2 mass fraction of 0.48 relative to the 0.97 value associated with the fully catalytic wall LAURA solution.

All heating predictions presented assume laminar flow. The freestream flight Reynolds number based on Microprobe's diameter is near 8×10^4 at maximum heating. Its maximum value is around 1×10^5. For Mars Pathfinder, a conservative value of 9×10^5 was selected as the transition flight Reynolds number[10] based on an examination of momentum thickness Reynolds numbers in the boudary layer. Based on Reynolds number effects, therefore, the forebody boundary layer should remain laminar. In addition, arcjet testing reveal that the mass blowing rates due to ablation associated with the expected heating rates are small, and the heatshield material [silicone-impegnated reusable ceramic ablator (SIRCA)] SIRCA/Split remains smooth during ablation so that heating augmentation due to transition to turbulence should not occur on the Microprobe forebody.

Undershoot Trajectory Heating Predictions

Computational heating predictions for the seven trajectory points listed in Table 2 are presented in Fig. 5. The calculations were computed on 30×64 grids. The maximum heating for this trajectory is 175.9 W/cm^2 at $t = 87.5$ s. Figure 6 compares the stagnation-point values from the seven solutions to the approximation of Eq. (1). The approximation is about 11% lower than the CFD predictions prior to the maximum heating and is approximately 18% above the CFD predictions after maximum heating. The integrated heat load from the approximation is 8712 J/cm^2. An estimate of the integrated heat load from the CFD solutions computed by fitting a similarly shaped curve through the points is 8860 J/cm^2.

Trajectory points prior to $t = 51.7$ s cannot be reliably predicted with continuum CFD methods such as LAURA. The Knudsen number associated with the 51.7-s trajectory point is 0.06. Reference 17 examines Microprobe heating in the rarefied flow regime.

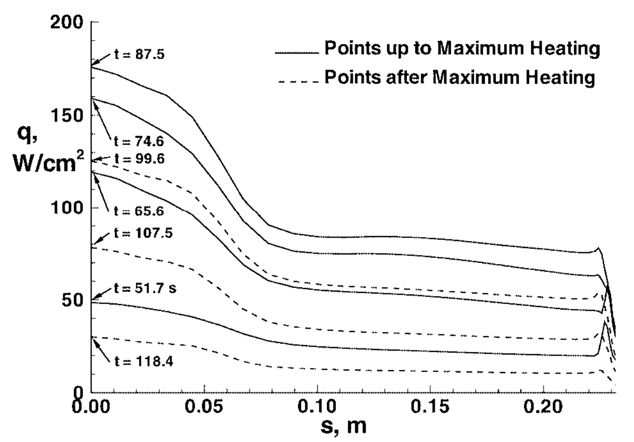

Fig. 5 Forebody heating distributions for seven overshoot trajectory points.

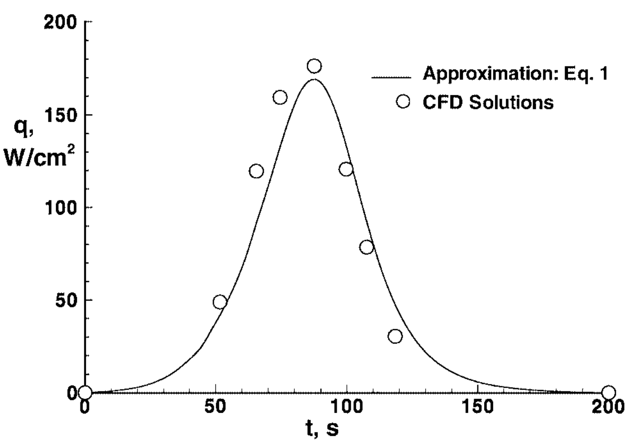

Fig. 6 Comparison of stagnation-point heating from CFD predictions to the approximation of Eq. (1) for the overshoot trajecory.

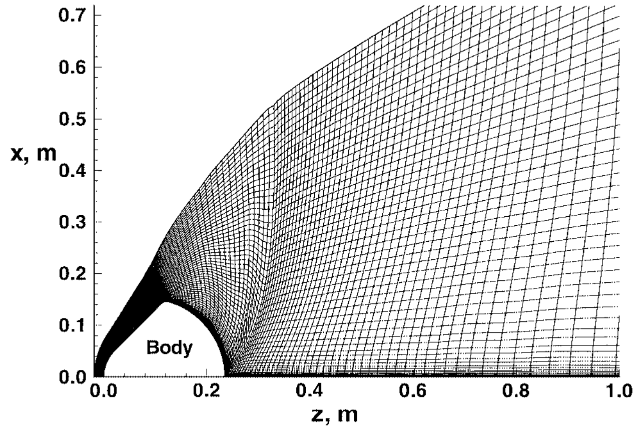

Fig. 7 Full vehicle axisymmetric 160 ×64 computational grid.

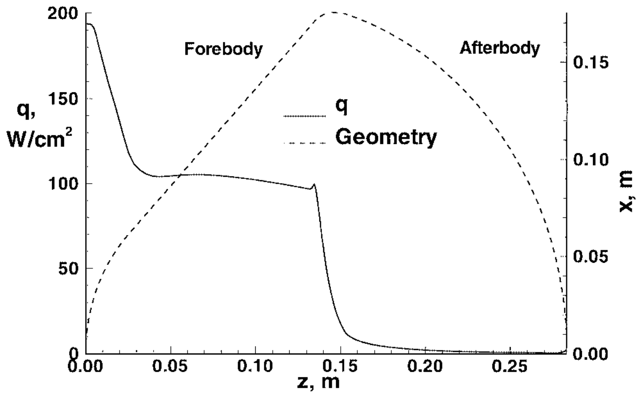

Fig. 8 Forebody and afterbody heating distributions for a maximum heating point in an undershoot trajectory.

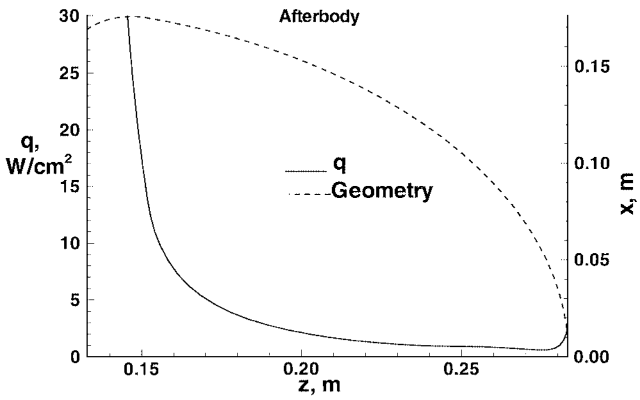

Fig. 9 Closeup of afterbody heating distributions for a maximum heating point in an undershoot trajectory.

Afterbody Heating

A zero angle-of-attack CFD solution was generated about the full vehicle to estimate heating on Microprobe's hemispherical afterbody. This calculation was performed at the maximum heating point from an undershoot trajectory and used the 160 × 64 grid shown in Fig. 7 (64 points normal to the surface). Figure 8 presents the predicted heating for the forebody and the afterbody. Figure 9 details the afterbody prediction. Heating drops rapidly around the shoulder to around 1% of the forebody stagnation-point value. The flow stays attached along most of the afterbody. Additional discussion of afterbody heating is contained in the next section.

Angle-of-Attack Effects

Because the Mars Microprobe may encounter the atmosphere of Mars at an uncertain orientation, the envelope of possible angles of attack early in the trajectory is large. From six-DOF Monte Carlo simulation, a plot of the expected total angles of attack as compared to the heat rates is shown in Fig. 10. At the point when stagnation-point heating rate is half of its maximum, the 3-sigma variation on total angle of attack is as large as 40 deg. These large angles of attack during the heating pulse need to be accounted for in design of the probe's TPS.

Figure 11 presents the Mach 6 thermographic phosphor measurements in the form of a heat transfer coefficient C_h normalized to the 0-deg angle-of-attack stagnation-point value $C_{h_{\mathrm{ref}}}$. The measurements were taken only on the windside of the vehicle. The measurements reveal that windside shoulder region heating ratio increases from 0.40 to 0.81 as angle of attack increases from 0 to 45 deg. Figure 12 shows a closeup of the afterbody region.

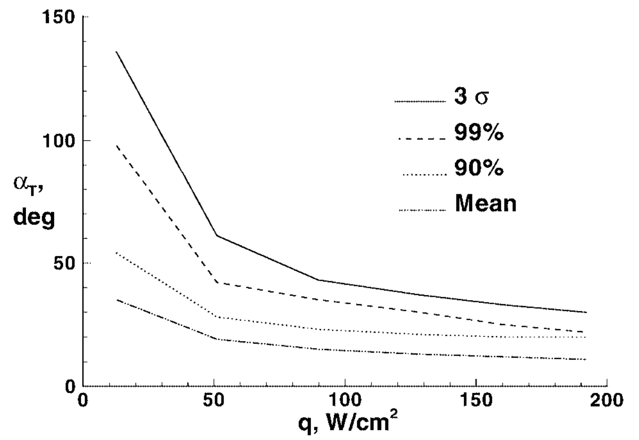

Fig. 10 Statistical variation in total angle of attack as a function of stagnation-point heat rate.

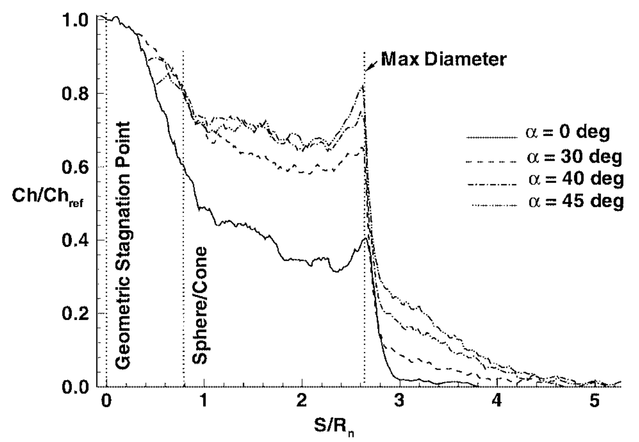

Fig. 11 Thermographic phosphor measurements of normalized heat transfer coefficient from NASA Langley Research Center 20-Inch Mach 6 Air Tunnel: *Re*/ft = 4.3 × 10^6.

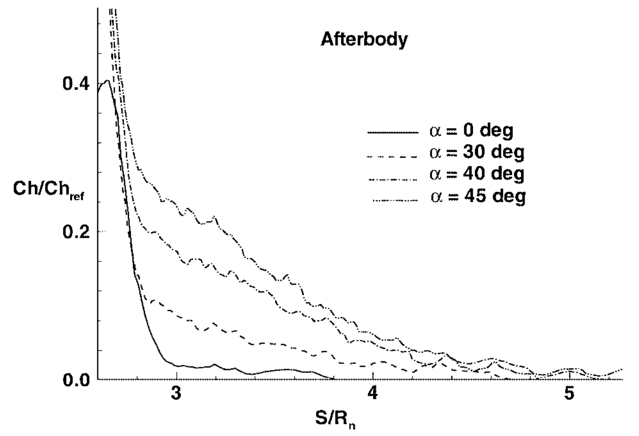

Fig. 12 Afterbody thermographic phosphor measurements of normalized heat transfer coefficient from NASA Langley Research Center 20-Inch Mach 6 Air Tunnel: *Re*/ft = 4.3 × 10^6.

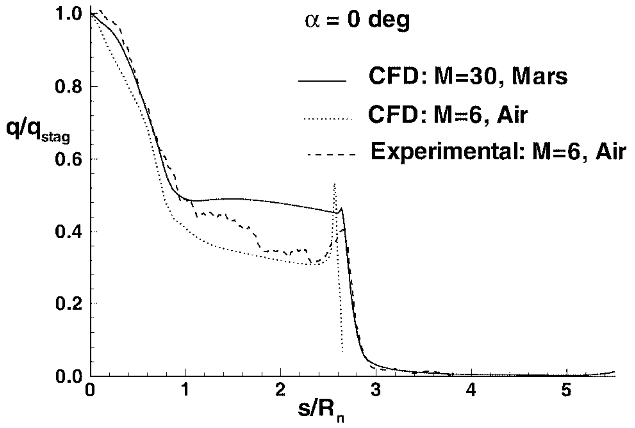

Fig. 13 Comparison of normalized heating predictions from CFD at Mach 30 in Mars atmosphere, perfect-gas CFD at Mach 6 in air, and measurements at Mach 6 in air.

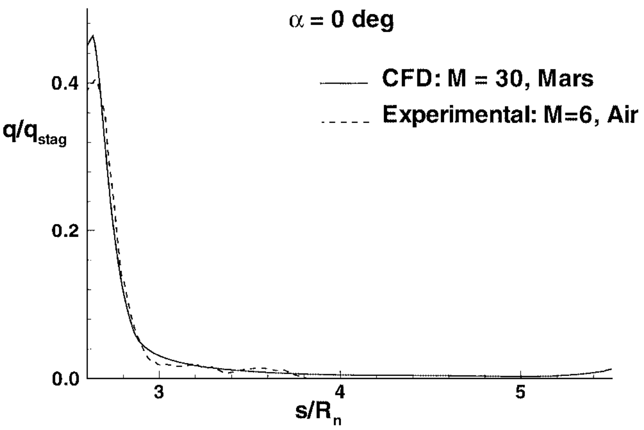

Fig. 14 Comparison of normalized afterbody heating predictions from CFD at Mach 30 in Mars atmosphere with measurements at Mach 6 in air.

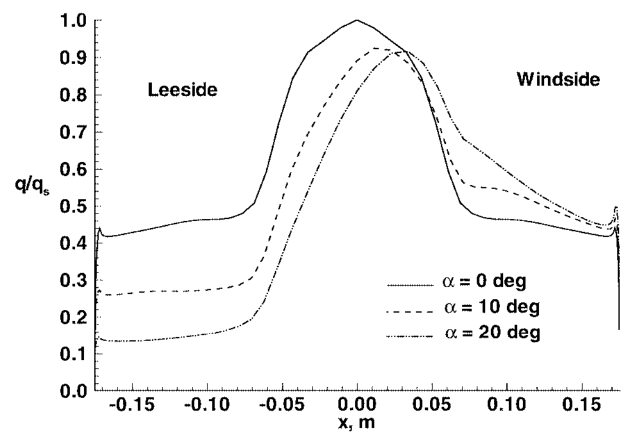

Fig. 15 Effect of angle of attack on normalized forebody heating across the symmetry plane from CFD predictions (Mars atmosphere).

Figure 13 compares the measured zero angle-of-attack normalized heating distributions to LAURA CFD predictions at Mach 30 Mars conditions discussed in the "Afterbody Heating" section. A CFD calculation for Mach 6 air (forebody-only calculation) is also included. Real-gas effects are evident on the forebody frustrum, where the Mars calculation predicts higher heating (relative to the stagnation-point value) than both the measured values and the Mach 6 air calculation. Figure 14 presents a closeup of the afterbody region.

Figure 15 presents forebody heating across the symmetry plane (normalized to the zero angle-of-attack stagnation-point value) from CFD predictions at 0-, 10-, and 20-deg angle of attack at a trajectory point near maximum heating in the nominal trajectory. On the windside (positive x in Fig. 15), the heating increases with angle of attack, and the qualitative nature of the distribution changes as a result of the shift of the sonic line from the nose to the shoulder. Leeside heating (negative x) is reduced with increased angle of attack.

The motion of the Microprobe during the heat pulse is an oscillation in angle of attack α and sideslip angle β. Figure 16 presents a representative trajectory showing the relationship between the aerodynamic angles and the heat pulse. To predict the expected maximum heating rate and heat load that the heatshield must be designed for, the information in Figs. 11, 15, and 16 may be combined. To make the problem tractable, seven points are selected on the Microprobe geometry, as shown in Fig. 17. Windside heating predictions in Figs. 11 and 15, as well as leeside predictions in Fig. 15, are used to estimate the heating at each of the seven points as a function of angle of attack. The actual motions from the trajectory in Fig. 16 can then be used to integrate the heat load at each of the points. (To assess heating for nonzero azimuthal points, a sinusoidal variation from windside to leeside is assumed.) The predicted heating at each of the points is given in Fig. 18 for the trajectory shown in Fig. 16. By repeating this methodology for all possible entry trajectories from a six-DOF Monte Carlo entry simulation, a statistical examination of the effect of angle of attack (as well as other off-nominal conditions simulated in the six-DOF) on heating at each of the seven points can be conducted. A summary of the results of this calculation is given in Table 4 for heat rate, in watts per square centimeters, and in Table 5

Table 4 Maximum heat transfer rate

Point	Minimum	Mean	Maximum	3-σ Deviation
1	166.3	178.8	201.8	13.3
2	100.6	112.4	130.7	11.4
3	83.3	93.2	108.6	9.45
4	79.2	87.1	100.7	7.88
5	9.76	11.66	16.0	2.28
6	1.67	2.75	7.15	3.3
7	3.34	3.69	6.05	0.94

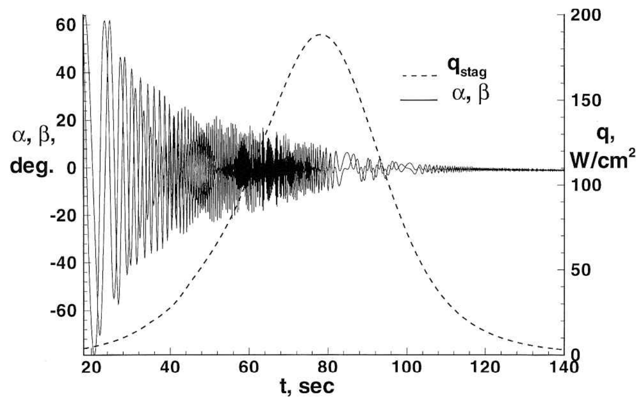

Fig. 16 Relationship between vehicle attitude angles and the heat pulse for one possible trajectory.

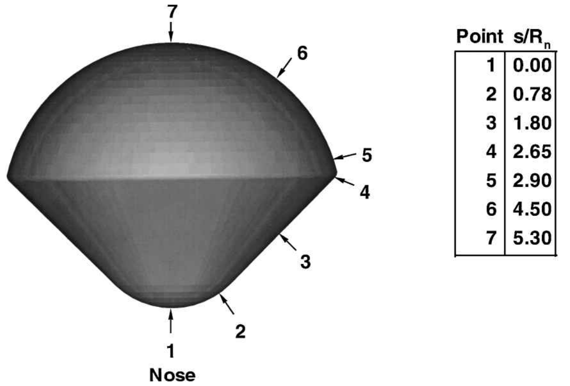

Fig. 17 Definition of seven selected points on vehicle for six-DOF heating tracking.

Table 5 Integrated heat load

Point	Minimum	Mean	Maximum	3-σ Deviation
1	7327	8112	8816	517
2	4130	4571	5003	306
3	3314	3706	4102	281
4	3217	3589	3943	247
5	438	509	595	91
6	82	103	147	36
7	164	193	244	46

Table 6 Ratios of angle-of-attack effects to zero angle of attack (mean trajectory)

Point	Maximum rate	Heat load
1	0.99	0.97
2	1.10	0.95
3	1.10	0.94
4	1.07	0.94
5	1.44	1.35
6	3.12	1.57
7	1.19	1.35

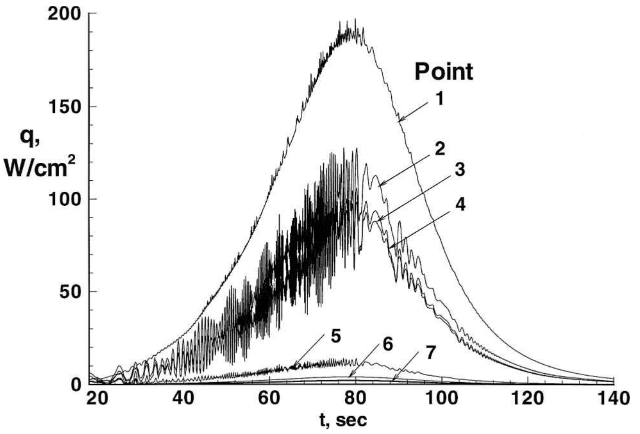

Fig. 18 Time history of heating at seven selected points on geometry for one possible trajectory.

for heat load, in joules per square centimeters, at seven points on the body from a six-DOF Monte Carlo analysis (with angle-of-attack effects).

Although the methodology used to generate Tables 4 and 5 is valid, the accuracy of the values presented is limited by the accuracy of the data used to establish the effect of angle of attack on heating distributions around the probe. In particular, the large angle-of-attack variation relies heavily on the Mach 6 air experimental measurements, whose applicability to this higher speed Mars entry is uncertain. In addition, leeside heating on the afterbody and azimuthal variations had to be estimated. The accuracy could be increased through a series of computationally expensive CFD calculations (including the wake) for the entire range of angles of attack.

Traditionally, planetary entry heatshield design utilized the maximum heat rate from the undershoot trajectory and the heat load from the overshoot trajectory while neglecting off-nominal angle-of-attack effects as well as other off-nominal conditions typically included in six-DOF Monte Carlo trajectory analysis. (Off-nominal conditions examined are discussed in Ref. 4.) To assess the effect of these off-nominal conditions, the 3-σ values from Tables 4 and 5 (mean value plus 3-σ deviation) can be compared with values predicted from traditional heatshield sizing approaches. This comparison, in the form of ratios of the 3-σ six-DOF values to the traditional value for both heat rate and heat load to each of the seven body points, is given in Table 6.

Table 6 shows that the effect of angle of attack and other off-nominal conditions increases the maximum heat rate predicted on much of the forebody by about 10% (except at the stagnation point) while decreasing the heat load to the forebody by 3–6%. On the afterbody, the heat rates can be as much as a factor of 3 higher with the associated heat loads increased by 30–60%.

Conclusions

Design of an efficient TPS for Mars Microprobes requires prediction of the expected aerothermal heating that the aeroshells will encounter during the hypersonic portion of their trajectory. A combination of computational predictions and experimental measurements is used to provide this prediction.

The maximum instantaneous heating rate at the vehicle's stagnation point (at zero angle of attack) is predicted using the CFD code LAURA to be 194 W/cm^2. This value is 3.6% higher than a Sutton–Graves approximation and is 7% higher than a VSL prediction. No significant heating augmentation due to radiation is expected. The forebody shock layer should remain laminar. Maximum stagnation-point pressure expected is 0.094 atm.

From computations at seven overshoot trajectory points (ballistic coefficient = 38 kg/m^2), the maximum heat load expected at the stagnation point is estimated to be 8800 J/cm^2.

Heat rates and heat loads on the vehicle's afterbody are much lower than the forebody. At 0-deg angle of attack, heating over much of the hemispherical afterbody is predicted to be less than 2% of the stagnation-point value.

Good qualitative agreement is demonstrated for zero angle-of-attack afterbody heating between CFD calculations at Mars entry conditions and experimental thermographic phosphor measurements from the NASA Langley Research Center 20-Inch Mach 6 Air Tunnel. On the forebody frustrum, the experimental data is as much as 30% lower than the Mars atmosphere CFD prediction.

The effect of angle of attack and other off-nominal conditions increases the maximum heat rate encountered on much of the forebody by about 10% while decreasing the heat load to that region by 3–6%. Angle of attack increases afterbody heating as much as a factor of 3 with associated heat loads increased by 30–60%.

Acknowledgments

Thanks are extended to Roop Gupta of NASA Langley Research Center for supplying the viscous shock layer heating estimate and Eric Slimko of the Jet Propulsion Laboratory for many helpful discussions.

References

[1]Powell, G., and Gavit, S., "New Millennium Mars Microprobe Mission and System Specifications," Jet Propulsion Lab., D-13752, NMP/Spec-02, California Inst. of Technology, Pasadena, CA, Sept. 1996.

[2]Weinberg, S. A., "Final Data Report—Pioneer-Venus Static and Dynamic Transonic Wind Tunnel Tests," General Electric Corp., 9154-TDM-75-013, Valley Forge, PA, July 1975.

[3]Mitcheltree, R. A., Moss, J. N., Cheatwood, F. M., Greene, F. A., and Braun, R. D., "Aerodynamics of the Mars Microprobe Entry Vehicles," *Journal of Spacecraft and Rockets*, Vol. 36, No. 3, 1999, pp. 392–398; also AIAA Paper 97-3658, Aug. 1997.

[4]Braun, R. D., Mitcheltree, R. A., and Cheatwood, F. M., "Mars Microprobe Entry-to-Impact Analysis," *Journal of Spacecraft and Rockets*, Vol. 36, No. 3, 1999, pp. 412–420; also *Proceedings from the 1997 IEEE Aerospace Conference*, 1997.

[5]Sutton, K., and Graves, R. A., "A General Stagnation-Point Convective-Heating Equation for Arbitrary Gas Mixtures," NASA TR-R-376, Nov. 1971.

[6]Gnoffo, P. A., "An Upwind-Biased, Point-Implicit Relaxation Algorithm for Viscous, Compressible Perfect-Gas Flows," NASA TP-2953, Feb. 1990.

[7]Mitcheltree, R. A., "Aerothermodynamic Methods for a Mars Environmental Survey Mars Entry," *Journal of Spacecraft and Rockets*, Vol. 31, No. 3, 1994, pp. 516–523.

[8]Braun, R. D., Powell, R. W., Engelund, W. C., Gnoffo, P. A., Weilmuenster, K. J., and Mitcheltree, R. A., "Mars Pathfinder Six-Degree-of-Freedom Entry Analysis," *Journal of Spacecraft and Rockets*, Vol. 32, No 6, 1996, pp. 993–1000.

[9]Mitcheltree, R. A., and Gnoffo, P. A., "Wake Flow About the Mars Pathfinder Entry Vehicle," *Journal of Spacecraft and Rockets*, Vol 32, No. 5, 1995, pp. 771–776.

[10]Mitcheltree, R. A., "Computational Aerothermodynamics for Mars Pathfinder Including Turbulence," AIAA Paper 95-3493, Aug. 1995.

[11]Gnoffo, P. A., Weilmuenster, K. J., Braun, R. D., and Cruz, C. I., " Influence of Sonic Line Location on Mars Pathfinder Aerodynamics," *Journal of Spacecraft and Rockets*, Vol. 33, No. 2, 1996, pp. 169–177.

[12]Gnoffo, P. A., Weilmuenster, K. J., Powell, R. W., Mitcheltree, R. A., Engelund, R. D., and Braun, R. D., "Prediction and Validation of Mars Pathfinder Hypersonic Aerodynamic Data Base," AIAA Paper 98-2445, June 1998.

[13]Micol, J. R., "Hypersonic Aerodynamic/Aerothermodynamic Testing Capabilities at Langley Research Center: Aerothermodynamic Facilities Complex," AIAA Paper 95-2107, June 1995.

[14]Merski, N. R., "Global Aeroheating Wind-Tunnel Measurements Using Improved Two-Color Phosphor Thermography Method," *Journal of Spacecraft and Rockets*, Vol. 36, No. 2, 1999, pp. 160–170.

[15]Tauber, M. E., and Sutton, K., "Stagnation-Point Heating Relations for Earth and Mars Entries," *Journal of Spacecraft and Rockets*, Vol. 28, No. 1, 1991, pp. 40–42.

[16]Gupta, R. N., Lee, K. P., Moss, J. N., and Sutton, K., "Viscous Shock Layer Analysis of the Martian Aerothermal Environment," *Journal of Spacecraft and Rockets*, Vol. 29, No. 5, 1992, pp. 633–640.

[17]Moss, J. N., Wilmoth, R. G., and Price, J. M., "Direct Simulation Monte Carlo Calculations of Aerothermodynamics for Mars Microprobe Capsules," *Journal of Spacecraft and Rockets*, Vol. 36, No. 3, 1999, pp. 399–404.

R. D. Braun
Guest Editor